

The Discovery of the W and Z Particles

Luigi Di Lella¹ and Carlo Rubbia²

¹*Physics Department, University of Pisa, 56127 Pisa, Italy*
luigi.di.lella@cern.ch

²*GSSI (Gran Sasso Science Institute), 67100 L'Aquila, Italy*
carlo.rubbia@cern.ch

This article describes the scientific achievements that led to the discovery of the weak intermediate vector bosons, W^\pm and Z, from the original proposal to modify an existing high-energy proton accelerator into a proton–antiproton collider and its implementation at CERN, to the design, construction and operation of the detectors which provided the first evidence for the production and decay of these two fundamental particles.

1. Introduction

The first experimental evidence in favour of a unified description of the weak and electromagnetic interactions was obtained in 1973, with the observation of neutrino interactions resulting in final states which could only be explained by assuming that the interaction was mediated by the exchange of a massive, electrically neutral virtual particle.¹ Within the framework of the Standard Model, these observations provided a determination of the weak mixing angle, θ_w , which, despite its large experimental uncertainty, allowed the first quantitative prediction for the mass values of the weak bosons, W^\pm and Z. The numerical values so obtained ranged from 60 to 80 GeV for the W mass, and from 75 to 92 GeV for the Z mass, too large to be accessible by any accelerator in operation at that time.

The ideal machine to produce the weak bosons and to measure their properties in the most convenient experimental conditions is an e^+e^- collider, as beautifully demonstrated by the success of the LEP program at CERN. However, while LEP was still far in the future, in 1976 Rubbia, Cline and McIntyre² proposed the transformation of an existing high-energy proton accelerator into a proton–antiproton collider as a quick and relatively cheap way to achieve collisions above threshold for W and Z production. In such a scheme a proton (p) and an anti-proton (\bar{p}) beam, each of energy E , circulate along the same magnetic path in opposite directions, providing head-on $\bar{p}p$ collisions at a total centre-of-mass energy $\sqrt{s} = 2E$.

Such a scheme was suggested both at Fermilab and CERN. It was adopted at CERN in 1978 for the 450 GeV proton synchrotron (SPS), and the first $\bar{p}p$ collisions at $\sqrt{s} = 540$ GeV were observed in July 1981. By the end of 1982, the $\bar{p}p$ collision

rate was high enough to permit the observation of $W \rightarrow e\nu$ decays. In a subsequent run during the spring of 1983, the decays $Z \rightarrow e^+e^-$ and $Z \rightarrow \mu^+\mu^-$ were also observed.

After a short description of the collider itself and of the two detectors, UA1 and UA2, which took data at this new facility, this article describes the experimental results which led to the first observation of the W and Z bosons. This major discovery was awarded the 1984 Nobel Prize for Physics.

2. The CERN Proton–Antiproton Collider

The conception, construction and operation of the CERN proton–antiproton collider was a great achievement in itself. It is useful, therefore, to give a short description of this facility.

The production of W and Z bosons at a $\bar{p}p$ collider is expected to occur mainly as the results of quark–antiquark annihilation $\bar{d}u \rightarrow W^+$, $d\bar{u} \rightarrow W^-$, $u\bar{u} \rightarrow Z$, $d\bar{d} \rightarrow Z$. In the parton model $\sim 50\%$ of the momentum of a high-energy proton is carried, on average, by three valence quarks, and the remainder by gluons. Hence a valence quark carries about $1/6$ of the proton momentum. As a consequence, W and Z production should require a $\bar{p}p$ collider with a total centre-of-mass energy equal to about six times the boson masses, or 500–600 GeV. The need to detect $Z \rightarrow e^+e^-$ decays determines the minimal collider luminosity: the cross-section for inclusive Z production at ~ 600 GeV is ~ 1.6 nb, and the fraction of $Z \rightarrow e^+e^-$ decays is $\sim 3\%$, hence a luminosity $L = 2.5 \times 10^{29} \text{ cm}^{-2}\text{s}^{-1}$ would give an event rate of ~ 1 per day. To achieve such luminosities one would need an antiproton source capable of delivering daily $\sim 3 \times 10^{10}$ \bar{p} distributed in few (3–6) tightly collimated bunches within the angular and momentum acceptance of the CERN SPS.

The CERN 26 GeV proton synchrotron (PS) is capable of producing antiprotons at the desired rate. The PS accelerates $\sim 10^{13}$ protons per pulse which are transported every 2.4 s to the \bar{p} production target. Approximately 7×10^6 \bar{p} with a momentum of 3.5 GeV/c are then produced at 0° in a solid angle of 8×10^{-3} sr in a momentum interval $\Delta p/p = 1.5\%$. These antiprotons are sufficient in number, but they occupy a phase space volume which is too large by a factor $\geq 10^8$ to fit into the SPS acceptance, even after acceleration to the SPS injection energy of 26 GeV. It is necessary, therefore, to increase the \bar{p} phase space density at least 10^8 times before sending the \bar{p} beam to the SPS. This process is called “cooling” because a bunch of particles occupying a large phase space volume appears as a hot gas, with large velocities in all directions, when viewed by an observer at rest in the centre-of-mass frame of the bunch itself.

The CERN collider project used the technique of stochastic cooling, invented by S. van der Meer in 1972.³ A central notion in accelerator physics is phase space, well-known from other areas of physics. An accelerator or storage ring has an acceptance that is defined in terms of phase space volume. Traditional particle

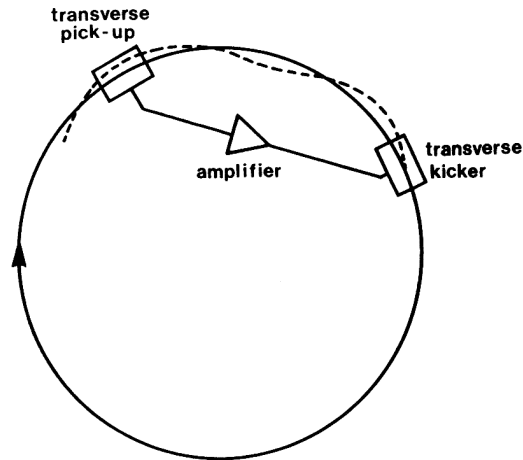


Fig. 1. Cooling of a single particle horizontal oscillation.

acceleration is generally dominated by the so-called Liouville theorem that forbids any compression of phase volume by conservative forces such as the electromagnetic fields that are used by accelerator builders. In fact, all that can be done in treating particle beams is to distort the phase space volume without changing the density anywhere. Already at MURA in the 1950s⁴ it was quickly realised that some beam phase-space compression was required from the source to the collisions (O'Neill, Piccioni, Symon).

The principle of stochastic cooling is illustrated in Fig. 1 for the cooling of horizontal “betatron” oscillations. Particles which do not follow exactly the central orbit in a magnetic ring undergo oscillations around the central orbit under the influence of focusing magnetic fields. A pick-up electrode mounted in a location where the oscillation amplitude is maximum provides a signal proportional to the particle distance from the central orbit. This signal is amplified and applied to a “kicker” mounted in a location where the particle crosses the central orbit. The signal must arrive at the kicker at the same time as the particle, hence the cable connecting pick-up electrode and kicker must follow as much as possible a straight path. In practice, the pick-up electrode measures the average distance of a group of particles from the central orbit, instead of a single particle. The size of this group depends on the sensitivity of the pick-up system, and especially on its frequency response.

The specific feature of the stochastic cooling is based on the fact that particles are points in phase space with empty spaces in between. We may push each particle towards the centre of the distribution, squeezing the empty space outwards. The small-scale density is strictly conserved, but in a macroscopic sense the particle density appears as increased. In this way, and maintaining the Liouville theorem, the information about the individual particle’s position can be used, pushing together

the individual particles against empty space. As a result the density in 6-dimensional phase space has been boosted by a factor as large as 10^9 using simple methods in which sensors acquiring electric signal from the particles are excited in order to influence the amplified pick-up signals.

In practice, the sensor will not see one particle, but a very large number (e.g. 10^6 to 10^{12}). Each particle's individual signal will be overlapped to the perturbing signal of the other particles. Fortunately, this effect is proportional to the square of the gain, whereas the cooling effect (each particle acting on itself) varies linearly with gain and one can choose it so that the cooling effect predominates.

Following the success of the so-called Initial Cooling Experiment (ICE)⁵ providing the experimental demonstration that stochastic cooling could indeed achieve the increase of \bar{p} phase space density required to detect the W and Z bosons, the CERN proton-antiproton collider project was approved on May 28, 1978.

For the CERN collider stochastic cooling is achieved in a purpose-built machine called Antiproton Accumulator (AA), which includes several independent cooling systems to cool both horizontal and vertical oscillations, and also to decrease the beam momentum spread (cooling of longitudinal motion), by using pick-up electrodes which provide signals proportional to Δp . The AA is a large aperture magnetic ring. A picture of the AA during construction is shown in Fig. 2. Figure 3 illustrates cooling and accumulation of a \bar{p} stack in the AA.



Fig. 2. View of the Antiproton Accumulator during construction.

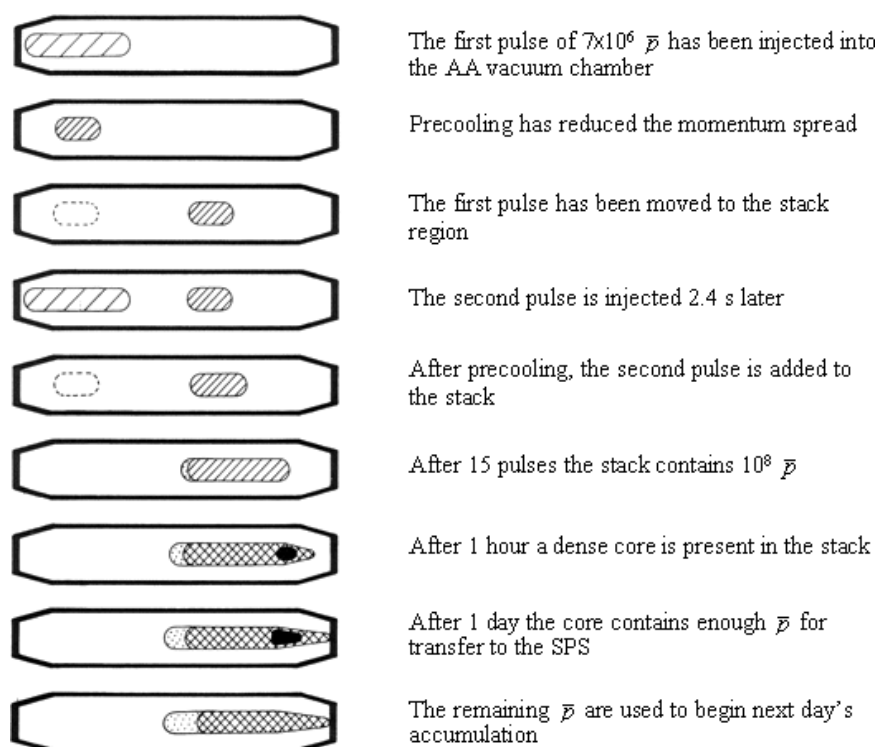


Fig. 3. Schematic sequence illustrating antiproton cooling and accumulation in the AA.

When a sufficiently dense \bar{p} stack has been accumulated in the AA, beam injection into the SPS is achieved using consecutive PS cycles. Firstly, three proton bunches (six after 1986), each containing $\sim 10^{11}$ protons, are accelerated to 26 GeV in the PS and injected into the SPS (see Fig. 4). Then three \bar{p} bunches (six after 1986), of typically $\sim 10^{10}$ \bar{p} each, are extracted from the AA and injected into the PS. Here they are accelerated to 26 GeV in a direction opposite to that of the protons, and then injected into the SPS. The relative injection timing of the bunches is controlled with a precision of ~ 1 ns to ensure that bunch crossing in the SPS occurs in the centre of the detectors.

The CERN experiment with proton-antiproton collisions has been the first storage ring in which bunched protons and antiprotons collided head on. Although the CERN proton-antiproton collider uses *bunched* beams, as do the e^+e^- colliders, a continuous phase-space damping due to synchrotron radiation is now absent. Furthermore, since antiprotons are scarce, one has to operate the collider in conditions of relatively large beam-beam interaction, which was not the case for the continuous proton beams of the previously operated Intersecting Storage Rings (ISR) at CERN.

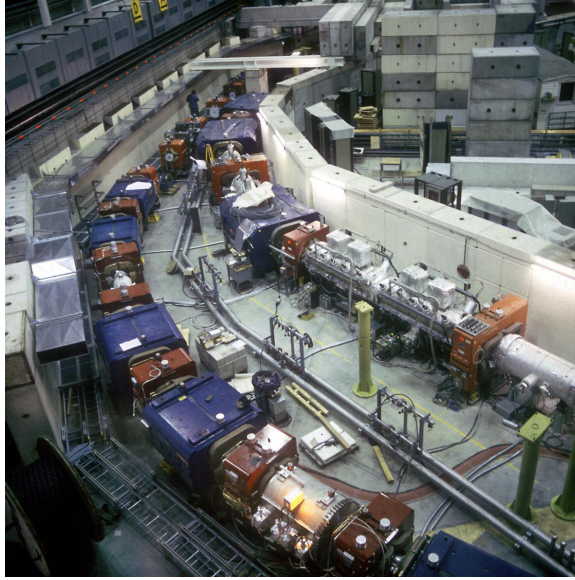


Fig. 5. View of the Antiproton Collector surrounding the Antiproton Accumulator.

Table 1 CERN proton–antiproton collider operation, 1981–1990.

Year	Collision energy (GeV)	Peak luminosity ($\text{cm}^{-2} \text{ s}^{-1}$)	Integrated luminosity (cm^{-2})
1981	546	$\sim 10^{27}$	2×10^{32}
1982	546	5×10^{28}	2.8×10^{34}
1983	546	1.7×10^{29}	1.5×10^{35}
1984–85	630	3.9×10^{29}	1.0×10^{36}
1987–90	630	3×10^{30}	1.6×10^{37}

pulses of $\sim 7 \times 10^7 \bar{p}$, thus increasing the \bar{p} stacking rate by a factor of ~ 10 . Table 1 summarises the evolution of the main collider parameters between 1981 (the first physics run) and 1990 (the last physics run). The collider was shut down at the end of 1990 because it was no longer competitive with the 1.8 TeV proton–antiproton collider at Fermilab which had started operation in 1987.

3. The Experiments

Since the SPS is built in an underground tunnel at an average depth of ~ 100 m, the project also required the excavation of underground experimental areas to house the detectors. The first experiment, named UA1 for “Underground Area 1” was soon

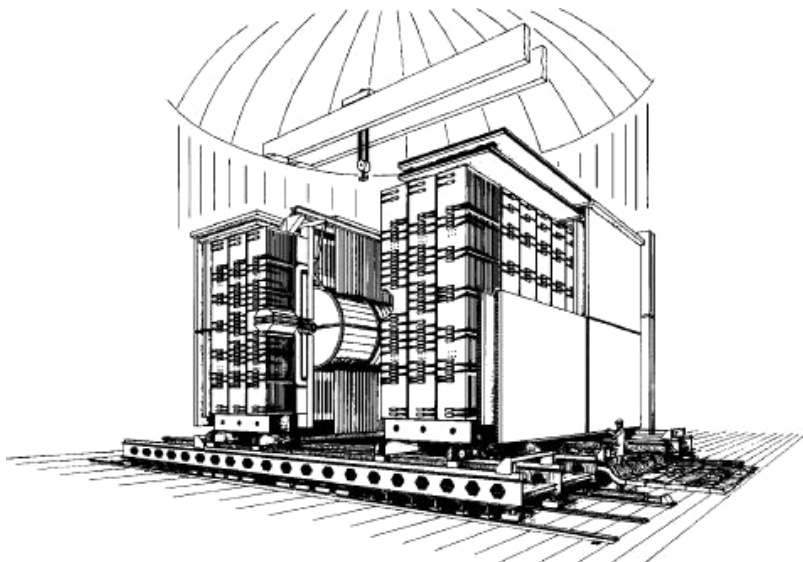


Fig. 6. View of the UA1 detector with the two magnet halves opened up.

approved on June 29, 1978. It was followed by a second experiment, named UA2, which was approved at the end of the same year.

3.1. The UA1 experiment

The UA1 experiment was designed as a general-purpose magnetic detector⁶ with an almost complete solid-angle coverage. A view of the detector with the two halves of the magnet opened up is shown in Fig. 6. The magnet is a dipole with a horizontal field of 0.7 T perpendicular to the beam axis over a volume of $7 \times 3.5 \times 3.5 \text{ m}^3$, produced by a warm aluminium coil to minimise absorption.

The magnet contains the central track detector, which is a system of drift chambers filling a cylindrical volume 5.8 m long with a 2.5 m diameter reconstructing charged particle trajectories down to polar angles of $\sim 6^\circ$ with respect to the beams. Tracks were sampled approximately every centimetre and could have up to 180 hits. This detector, at the cutting edge of technology in those days, was surrounded by electromagnetic and hadronic calorimeters down to 0.2° to the beam line. This “hermeticity”, as it was called later, turned out to be very effective to reconstruct undetected neutrinos from $W \rightarrow e\nu$ decay, and also to search for possible new, as yet undiscovered neutral particles escaping direct detection. It became one of the basic features of all general-purpose detectors at the next-generation e^+e^- and hadron colliders (LEP, the Fermilab $\bar{p}p$ collider and the LHC).

Electromagnetic calorimeters, consisting of Pb–scintillator multi-layer sandwich are also mounted inside the magnet. In the central region, they consist of two

cylindrical half-shells surrounding the tracker, each subdivided into 24 elements (“gondolas”) covering 180° in ϕ and 24 cm along the beam line, with a total thickness of 26.4 radiation lengths (X_0). Two similar structures are present at smaller angles to the beam line, each consisting of 32 radial sectors. The energy resolution for electrons was $\sigma(E)/E = 0.15/\sqrt{E}$ (E in GeV).

The magnet return yoke, and two iron walls located symmetrically at the two ends of the magnet, are laminated and scintillator is inserted between the iron plates to form a hadronic calorimeter, which is subdivided into 450 independent cells. Muon detectors, consisting of systems of drift tubes, surround the magnet yoke. The momentum resolution for a 40 GeV/ c muon track is typically $\pm 20\%$ (for comparison, the energy resolution for a 40 GeV electron, as measured by the electromagnetic calorimeter, is $\pm 2.5\%$).

In the days of initial construction, the UA1 collaboration consisted of about 130 physicists from Aachen, Annecy, Birmingham, CERN, Collège de France, Helsinki, London (QMC), UCLA-Riverside, Rome, RAL, Saclay and Vienna. In the history of particle physics, it was the first time that so many physicists were seen to work together on a common project, thus paving the way to the much larger collaborations of the LEP and LHC experiments in the following years.

A picture of UA1 during assembly is shown in Fig. 7.

Despite the general scepticism in the particle physics community that such a complex detector could be built and operated in time, it was essentially functional by the summer of 1981, in time for the first physics run.

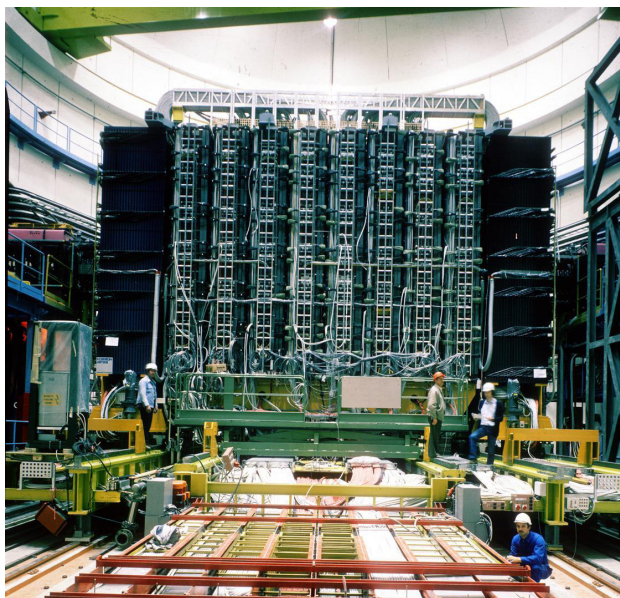


Fig. 7. The UA1 detector during assembly.

3.2. The UA2 detector

UA2 was not designed as a general-purpose detector, but rather optimised for the detection of electrons from W and Z decays. The emphasis was on highly granular calorimetry with spherical projective geometry, which was well adapted also to the detection of hadronic jets.

Figure 8 shows the layout of the UA2 detector for the collider runs between 1981 and 1985.⁷ The central region contains a “vertex detector”, which consists of various types of cylindrical tracking chambers. A “preshower” counter, located just behind the last chamber, and consisting of a tungsten cylinder followed by a multi-wire proportional chamber, is crucial for electron identification. The vertex detector is surrounded by the central calorimeter, which covers the full azimuth and is subdivided into 240 independent cells, each subtending the angular interval $\Delta\theta \times \Delta\phi = 10^\circ \times 15^\circ$ and consisting of an electromagnetic (Pb-scintillator) and a hadronic (Fe-scintillator) section. The calorimeter energy resolution for electrons was $\sigma(E)/E = 0.14/\sqrt{E}$ (E in GeV), and was $\sim 10\%$ for an 80 GeV hadron in the central calorimeters. There is no magnetic field in this region.

The two forward detectors, covering the polar angle interval between 20° and 37.5° with respect to the beams, consist of twelve azimuthal sectors in which a toroidal magnetic field is generated by twelve coils equally spaced in azimuth. Each sector includes tracking chambers, a “preshower” detector and an electromagnetic

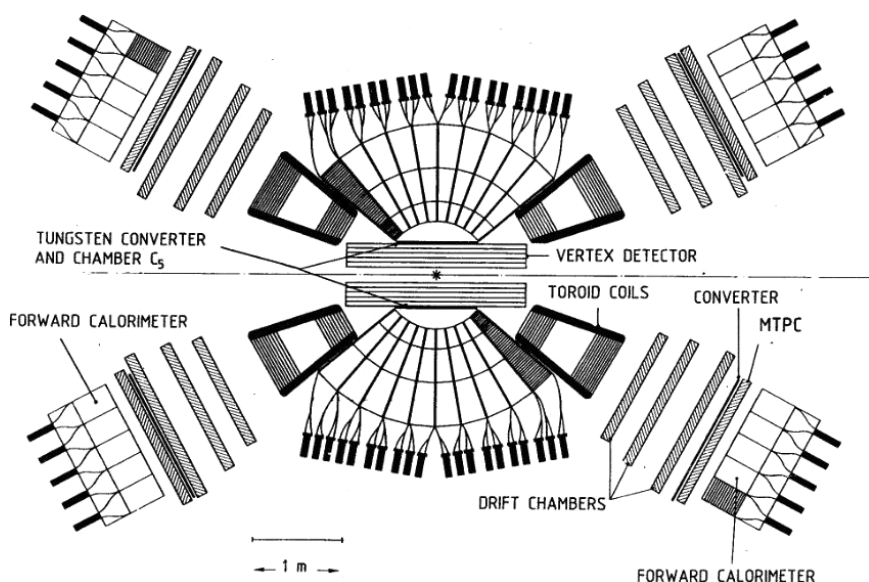


Fig. 8. Sketch of the UA2 detector in the 1981–85 configuration.

calorimeter. There is no muon detector in UA2. The initial UA2 collaboration consisted of about 60 physicists from Bern, CERN, Copenhagen, Orsay, Pavia and Saclay.

For the initial running (1981–83) the azimuthal coverage of the central calorimeter was 300° , with an interval of $\pm 30^\circ$ around the horizontal plane being covered by a single arm magnetic spectrometer at 90° to the beams.

At the end of 1985, the two forward magnetic detectors were replaced by calorimeters with full angular coverage down to 5° to the beams, thus greatly improving the detector hermeticity. These calorimeters were subdivided into cells with segmentation similar to that of the central calorimeter, and contained both an electromagnetic and a hadronic section. The central tracker was also upgraded, with silicon pad detectors, trackers and preshower counter made of scintillating fibres, and drift chambers detecting X-rays from the transition radiation produced by electrons in traversing many thin Lithium layers. This detector took data between 1987 and 1990. Figure 9 displays a picture of UA2 in the 1987–90 configuration. At that time groups from Cambridge, Heidelberg, Milano, Perugia and Pisa had joined the collaboration which had grown to about 100 physicists.

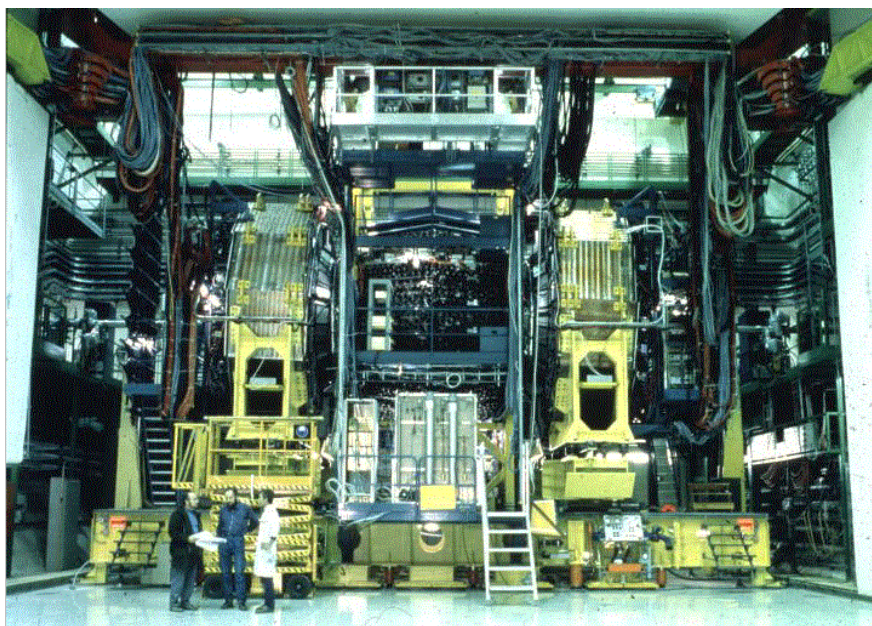


Fig. 9. The UA2 detector in the 1987–90 configuration.

4. The Discovery of the W and Z Bosons

The first physics run of the CERN collider took place at the end of 1981. The total integrated luminosity recorded by the two experiments during that run was not yet sufficient to detect the W and Z bosons, but that run demonstrated that there were no conceptual obstacles to further increase the luminosity to the required values by a careful tuning of all the machines involved in the collider operation (PS, AA, SPS) and of the interconnecting beam transfer lines. In those days the CERN collider caught the attention not only of the scientific community, but also of a part of the public opinion. The physics results from the 1982 and 1983 collider runs were eagerly awaited, as demonstrated by the many articles on this subject appearing in the world press. There was even the British Prime Minister, Margaret Thatcher, who asked the CERN Director-General to be personally informed of the W and Z discovery before the public announcements.

4.1. Discovery of the W boson

The W boson decays predominantly ($\sim 70\%$) to quark–antiquark pairs ($q\bar{q}'$), which appear as two hadronic jets. Such configurations are overwhelmed by two-jet production from hard parton scattering,⁸ hence both experiments have chosen to detect the W by identifying its leptonic decays: $W^\pm \rightarrow e^\pm \nu_e(\bar{\nu}_e)$ in both UA1 and UA2, and $W^\pm \rightarrow \mu^\pm \nu_\mu(\bar{\nu}_\mu)$ in UA1 only.

The signal from $W \rightarrow e\nu_e$ decay is expected to have the following features:

- the presence of a high transverse momentum (p_T) isolated electron;
- a peak in the electron p_T distribution at $m_W/2$ (the “Jacobian” peak);
- the presence of high missing transverse momentum from the undetected neutrino.

These features are the consequence of the main mechanism of W production (quark–antiquark annihilation), which results mainly in W bosons almost collinear with the beam axis, hence the decay electron and neutrino emitted at large angles to the beam axis have large p_T . We note that the missing longitudinal momentum cannot be measured at hadron colliders because of the large number of high-energy secondary particles emitted at very small angles to the beam which cannot be detected because their trajectories are inside the machine vacuum pipe.

The missing transverse momentum vector (\vec{p}_T^{miss}) is defined as

$$\vec{p}_T^{\text{miss}} = - \sum_{\text{cells}} \vec{p}_T$$

where \vec{p}_T is the transverse component of a vector associated with each calorimeter cell, with direction from the event vertex to the cell centre and length equal to the energy deposition in that cell, and the sum is extended to all cells with an energy deposition larger than zero. In an ideal detector with no measurement errors, for events with an undetected neutrino in the final-state it follows

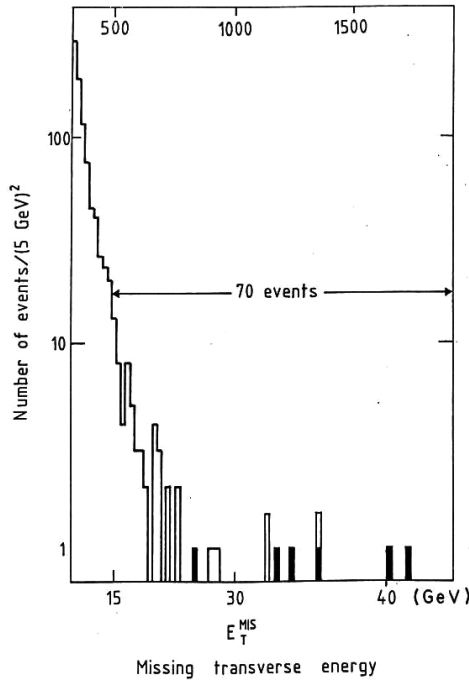


Fig. 10. UA1 distribution of the missing transverse momentum (called E_T^{MIS} in this plot) for equal bins of $(E_T^{\text{MIS}})^2$. The events shown as dark areas in this plot contain a high p_T electron.

from momentum conservation that \vec{p}_T^{miss} is equal to the neutrino transverse momentum.

Figure 10 shows the $|\vec{p}_T^{\text{miss}}|$ distribution, as measured by UA1 from the 1982 data.⁹ There is a component decreasing approximately as $|\vec{p}_T^{\text{miss}}|^2$ due to the effect of calorimeter resolution in events without significant $|\vec{p}_T^{\text{miss}}|$, followed by a flat component due to events with genuine $|\vec{p}_T^{\text{miss}}|$. Six events with high $|\vec{p}_T^{\text{miss}}|$ in the distribution of Fig. 10 contain a high- p_T electron. The \vec{p}_T^{miss} vector in these events is almost back-to-back with the electron transverse momentum vector, as shown in Fig. 11. These events are interpreted as due to $W \rightarrow e\nu_e$ decay. This result was first announced at a CERN seminar on January 20, 1983. Figure 12 shows the graphics display of one of these events.

The results from the UA2 search for $W \rightarrow e\nu$ events¹⁰ was presented at a CERN seminar on the following day (January 21, 1983). Six events containing an electron with $p_T > 15 \text{ GeV}/c$ were identified among the 1982 data. Figure 13 shows the distribution of the ratio between $|\vec{p}_T^{\text{miss}}|$ and the electron p_T for these events. Also shown in Fig. 13 is the electron p_T distribution for the events with a $|\vec{p}_T^{\text{miss}}|$ value comparable to the electron p_T (four events). These events have the properties expected from $W \rightarrow e\nu$ decay.

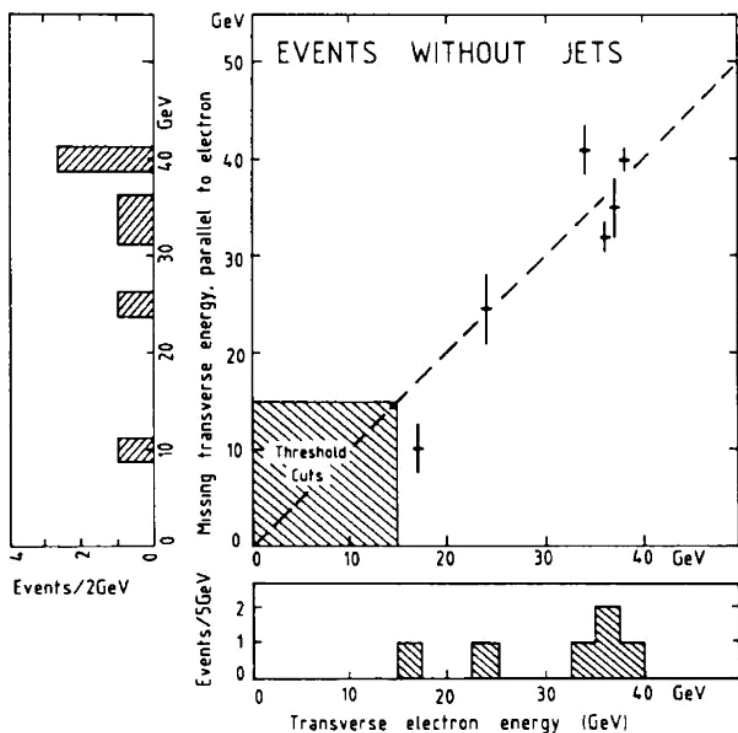


Fig. 11. UA1 scatter plot of all the events from the 1982 data which contain a high- p_T electron and large $|\vec{p}_T^{\text{miss}}|$. The abscissa is the electron $|\vec{p}_T|$ and the ordinate is the \vec{p}_T^{miss} component antiparallel to the electron \vec{p}_T .

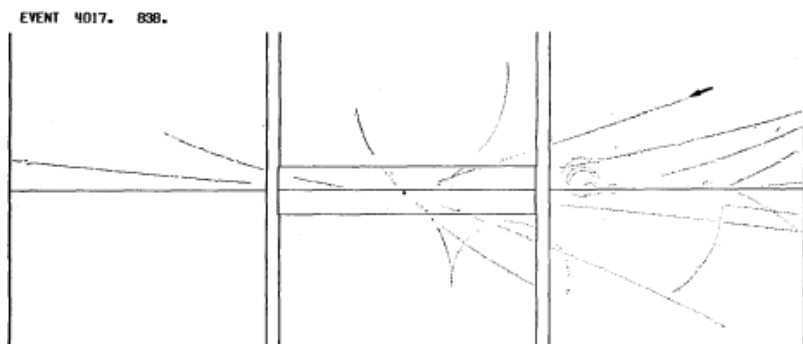


Fig. 12. Display of a UA1 $W \rightarrow e\nu$ event. The arrow points to the electron track.

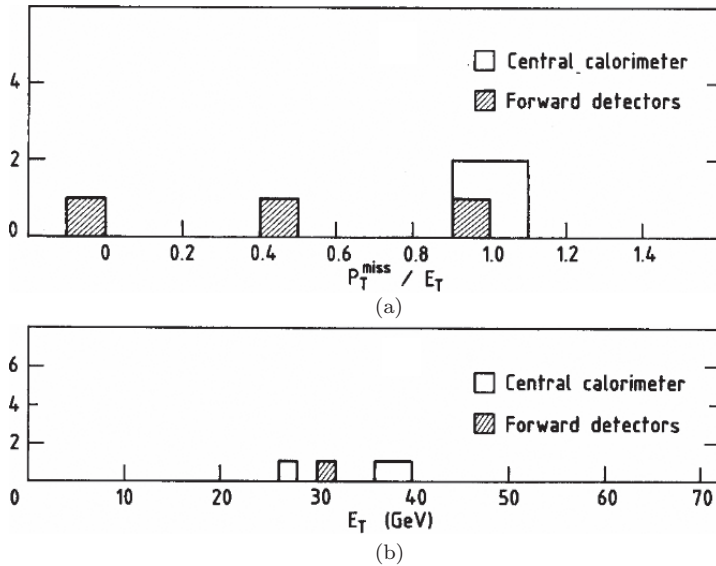


Fig. 13. (a) Display of the ratio between $|\vec{p}_T^{\text{miss}}|$ and the electron transverse momentum (called E_T in this plot) for six UA2 events containing an electron with $E_T > 15$ GeV; (b) Electron distribution for the four events with the highest $|\vec{p}_T^{\text{miss}}|/E_T$ ratio.

4.2. Discovery of the Z boson

Figure 14 illustrates the search for the decay $Z \rightarrow e^+e^-$ in UA1.¹¹ The first step of the analysis requires the presence of two calorimeter clusters consistent with electrons and having a transverse energy $E_T > 25$ GeV. Among the data recorded during the 1982–83 collider run, 152 events are found to satisfy these conditions. The next step requires the presence of an isolated track with $p_T > 7$ GeV/ c pointing to at least one of the two clusters. Six events satisfy this requirement, showing already a clustering at high invariant mass values, as expected from $Z \rightarrow e^+e^-$ decay. Of these events, four are found to have an isolated tracks with $p_T > 7$ GeV/ c pointing to both clusters. They are consistent with a unique value of the e^+e^- invariant mass within the calorimeter resolution. One of these events is displayed in Fig. 15.

An event consistent with the decay $Z \rightarrow \mu^+\mu^-$ was also found by UA1 among the data collected in 1983 (see Fig. 16). Figure 17 shows the mass distribution of all lepton pairs found by UA1 from the analysis of the 1982–83 data. The mean of these values is

$$m_Z = 95.2 \pm 2.5 \pm 3.0 \text{ GeV}$$

where the first error is statistical and the second one originates from the systematic uncertainty on the calorimeter energy scale.

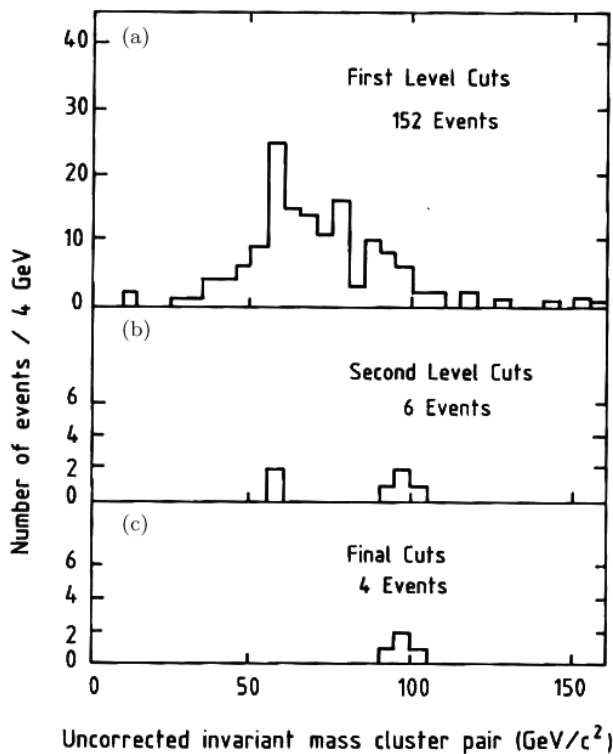


Fig. 14. Search for the decay $Z \rightarrow e^+e^-$ in UA1 (see text).

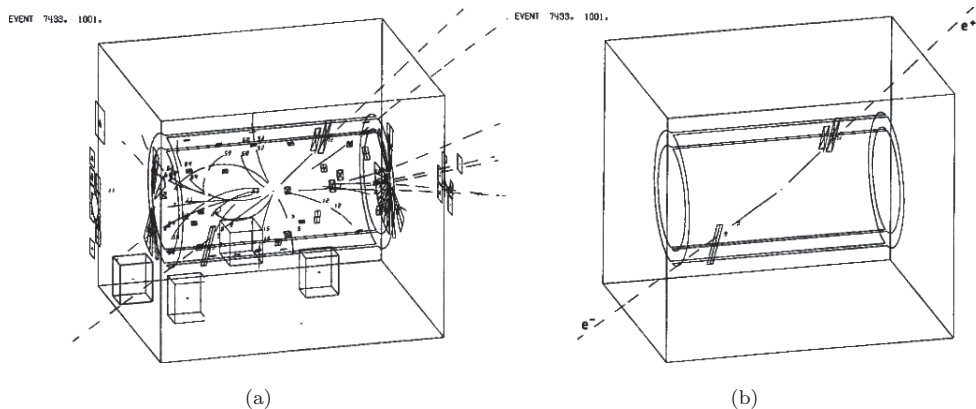


Fig. 15. One of the $Z \rightarrow e^+e^-$ events in UA1: (a) display of all reconstructed tracks and calorimeter hit cells; (b) only tracks with $p_T > 2 \text{ GeV}/c$ and calorimeter cells with $E_T > 2 \text{ GeV}$ are shown.

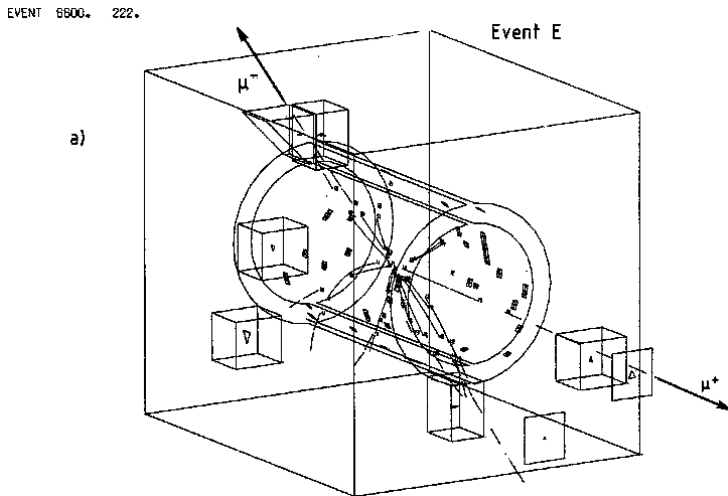
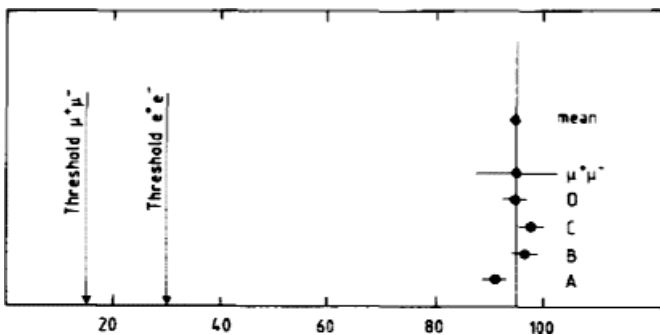
Fig. 16. $Z \rightarrow \mu^+ \mu^-$ event in UA1.

Fig. 17. Invariant mass distribution of all lepton pairs found by UA1 in the 1982–83 data.

The UA2 search for the decay $Z \rightarrow e^+ e^-$ among the 1982–83 data¹² is illustrated in Fig. 18. First, pairs of energy depositions in the calorimeter consistent with two isolated electrons and with $E_T > 25$ GeV are selected. Then, an isolated track consistent with an electron (from preshower information) is required to point to at least one of the clusters. Eight events satisfy these requirements: of these, three events have isolated tracks consistent with electrons pointing to both clusters. The weighted average of the invariant mass values for the eight events is

$$m_Z = 91.9 \pm 1.3 \pm 1.4 \text{ GeV}$$

where the first error is statistical and the second one originates from the systematic uncertainty on the calorimeter energy scale. The latter is smaller than the corresponding UA1 value because the smaller size of the UA2 calorimeter, and

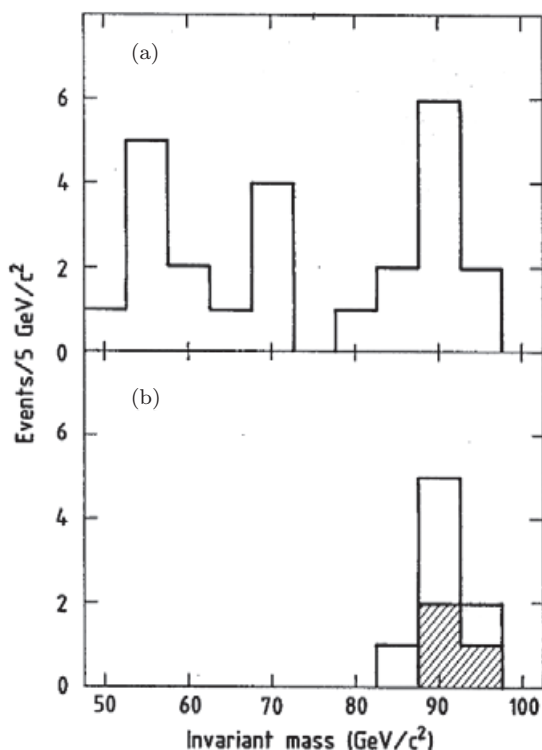


Fig. 18. Search for the decay $Z \rightarrow e^+e^-$ in UA2 (see text). The shaded area shows the three events with isolated electron tracks pointing to both calorimeter energy clusters.

its modularity, allow frequent recalibrations on electron beams of known energies from the CERN SPS.

Figure 19 shows the energy deposited in the UA2 calorimeter by a $W \rightarrow e\nu$ and by a $Z \rightarrow e^+e^-$ event. Such distributions, usually called “Lego plots”, illustrate the remarkable topologies of such events, with large amounts of energy deposited in a very small number of calorimeter cells, and little or no energy in the remaining cells.

5. Physics Results from Subsequent Collider Runs

Following the historical runs in 1982–83 which led to the discovery of the W and Z bosons, additional runs took place in the following years.

In a first phase, up to the end of 1985, with the two detectors basically unchanged, the collider energy was raised from $\sqrt{s} = 540$ GeV to 630 GeV and the peak luminosity doubled (see Section 2, Table 1). The new data allowed more detailed studies of the W and Z production and decay properties, beautifully confirming the Standard Model expectations.

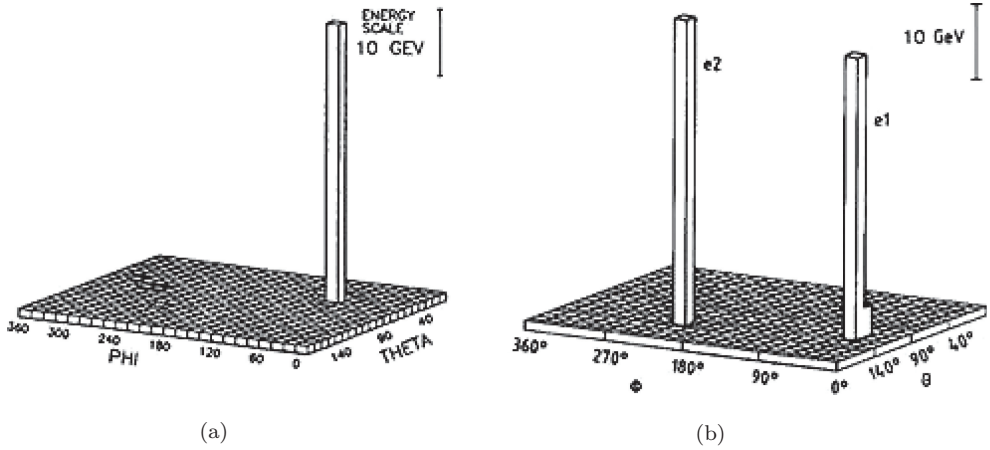


Fig. 19. The energy deposited in the UA2 calorimeter for a $W \rightarrow e\nu$ (a) and a $Z \rightarrow e^+e^-$ event (b).

As mentioned in Section 2, more physics runs took place at the CERN Collider between 1987 and its shut-down at the end of 1990. Other important physics results obtained by the two experiments between 1982 and 1990 are described in the next sub-sections.

5.1. W and Z masses and production cross-sections

At the end of 1985 UA1 had recorded 290 $W \rightarrow e\nu$, 33 $Z \rightarrow e^+e^-$, 57 $W \rightarrow \mu\nu$ and 21 $Z \rightarrow \mu^+\mu^-$ events.¹³ As an example, Fig. 20 shows the $W \rightarrow e\nu$ transverse mass (M_T) distribution, where $M_T = [2p_T^e p_T^\nu (1 - \cos \phi_{e\nu})]^{1/2}$, and $\phi_{e\nu}$ is the azimuthal separation between electron and neutrino (the transverse mass is used instead of the electron transverse momentum because its distribution is less sensitive to the W transverse momentum).

Figure 21 shows the invariant mass distribution of all e^+e^- pairs recorded by UA1 during the same period. The W and Z mass values obtained from fits to the distributions of Figs. 20 and 21 were

$$m_W = 82.7 \pm 1.0 \pm 2.7 \text{ GeV},$$

$$m_Z = 93.1 \pm 1.0 \pm 3.1 \text{ GeV},$$

where the first error is statistical and the second one reflects the uncertainty on the calorimeter energy scale.

The W and Z production cross-sections, multiplied with the corresponding decay branching ratios (BR), as measured by UA1, were

$$\sigma_W \text{BR}(W \rightarrow e\nu) = 630 \pm 50 \pm 100 \text{ pb};$$

$$\sigma_Z \text{BR}(Z \rightarrow e^+e^-) = 74 \pm 14 \pm 11 \text{ pb}.$$

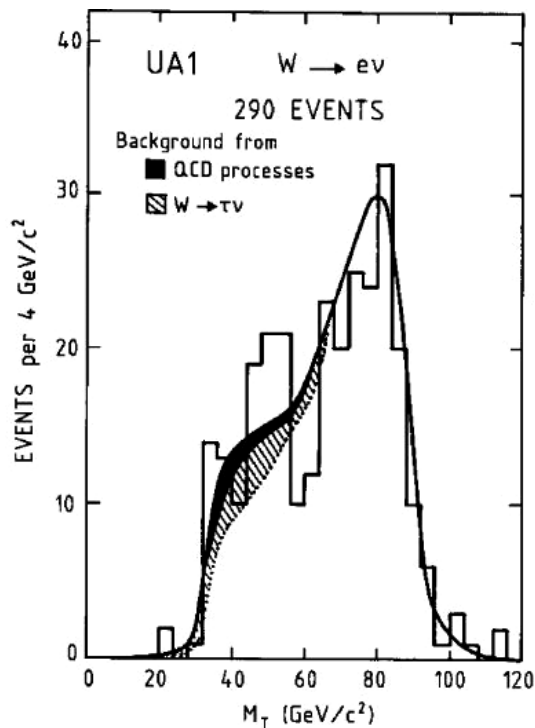


Fig. 20. Transverse mass distribution for all $W \rightarrow e\nu$ events recorded by UA1 between 1982 and 1985.

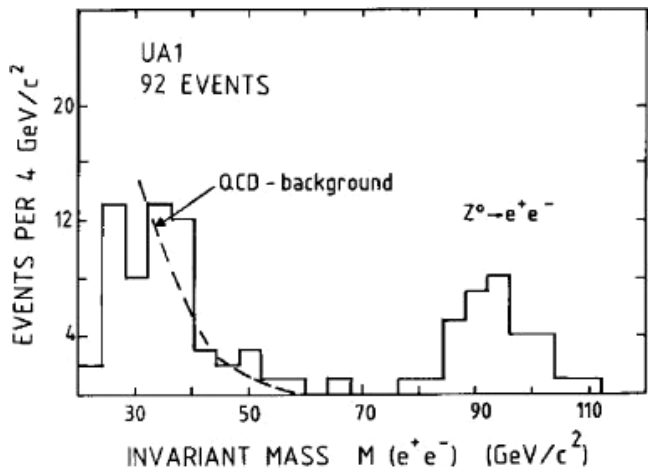


Fig. 21. Invariant mass distribution of all e^+e^- pairs recorded by UA1 between 1982 and 1985.

UA1 has also observed 32 $W \rightarrow \tau\nu$ decays followed by τ hadronic decay.¹⁴ These events appear in the detector has a highly collimated, low multiplicity hadronic jet approximately back-to-back in azimuth to a significant missing p_T .

In the same physics runs, from 1982 to 1985, the UA2 experiment had recorded samples of 251 $W \rightarrow e\nu$ and 39 $Z \rightarrow e^+e^-$ events.¹⁵ The measured properties of these events were in good agreement with the UA1 results. The W and Z mass values, as measured by UA2, were

$$m_W = 80.2 \pm 0.8 \pm 1.3 \text{ GeV},$$

$$m_Z = 91.5 \pm 1.2 \pm 1.7 \text{ GeV},$$

where, as usual, the first error is statistical and the second one reflects the uncertainty on the calorimeter energy scale.

5.2. Charge asymmetry in the decay $W \rightarrow e\nu$

At the energies of the CERN $\bar{p}p$ collider, W production is dominated by $q\bar{q}$ annihilation involving at least one valence quark or antiquark. As a consequence of the $V-A$ coupling, which violates parity conservation, the helicity of the quarks (antiquarks) is -1 ($+1$) and the W is almost fully polarised along the \bar{p} beam. Similar helicity arguments applied to $W \rightarrow e\nu$ decay predict that the leptons (e^- , μ^- , ν) should be preferentially emitted opposite to the direction of the W polarisation, and antileptons (e^+ , μ^+ , $\bar{\nu}$) along it.

The angular distribution of the charged lepton in the W rest frame can be written as

$$\frac{dn}{d\cos\theta^*} \propto (1 + q\cos\theta^*)^2$$

where θ^* is the angle of the charged lepton measured with respect to the W polarisation, and $q = -1$ ($+1$) for electrons (positrons). This axis is practically collinear with the incident \bar{p} direction if the W transverse momentum is small.

A complication arises from the fact that the neutrino longitudinal momentum is not measured, and the requirement that the invariant mass of the $e\nu$ pair be equal to the W mass gives two solutions for θ^* . The UA1 analysis¹³ retains only those events for which one solution is unphysical (W longitudinal momentum inconsistent with kinematics), and the lepton charge sign is unambiguously determined. Figure 22 shows the distribution of the variable $q\cos\theta^*$ for 149 unambiguous events. The distribution agrees with the expected $(1 + q\cos\theta^*)^2$ form. It must be noted that this result cannot distinguish between $V-A$ and $V+A$ because in the latter case all helicities change sign and the angular distribution remains the same.

5.3. A test of QCD: The W boson transverse momentum

To lowest order the W and Z bosons produced by $q\bar{q}$ annihilation are emitted with very low transverse momentum. However, gluon radiation from the initial

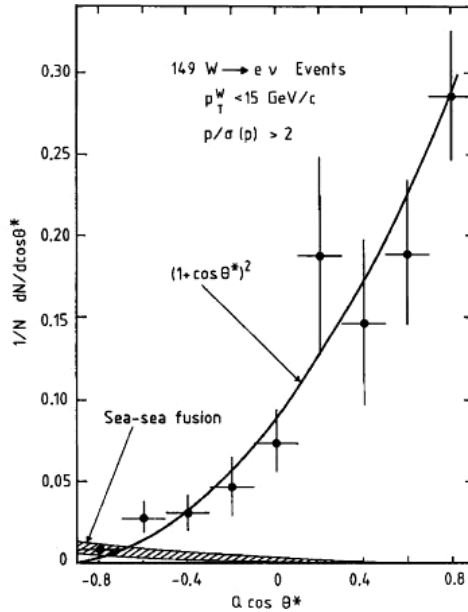


Fig. 22. Decay angular distribution for the final UA1 $W \rightarrow e\nu$ event sample (see text). The shaded band shows the expected contribution of wrong polarisation from the annihilation of a sea quark with a sea antiquark.

quarks (or antiquarks) may result in W and Z production with a sizeable transverse momentum, which is equal and opposite to the total transverse momentum of all hadrons produced in association with the intermediate bosons.

Figure 23 shows distributions of the W transverse momentum, p_T^W , as measured by UA1¹³ using the $W \rightarrow e\nu$ event sample. A QCD prediction,¹⁶ also shown in Fig. 23, agrees with the data over the full p_T^W range. The W bosons produced with high p_T^W are expected to recoil against one or more jets, and such jets are indeed observed experimentally.

5.4. Hadronic decays of the W and Z bosons

As mentioned earlier (see Section 4), the W and Z bosons decay predominantly ($\sim 70\%$) to quark–antiquark pairs which appear as two hadronic jets. Such configurations are overwhelmed by the QCD background of two-jet production from hard parton scattering. However, despite the unfavourable signal-to-noise ratio, the detection of $W \rightarrow q\bar{q}'$ and $Z \rightarrow q\bar{q}$ decays at the collider was considered as interesting not only as an experimental challenge, but also as a demonstration that the reconstruction of the two-jet invariant mass at next-generation hadron colliders could be useful to detect new particles decaying to two hadronic jets.

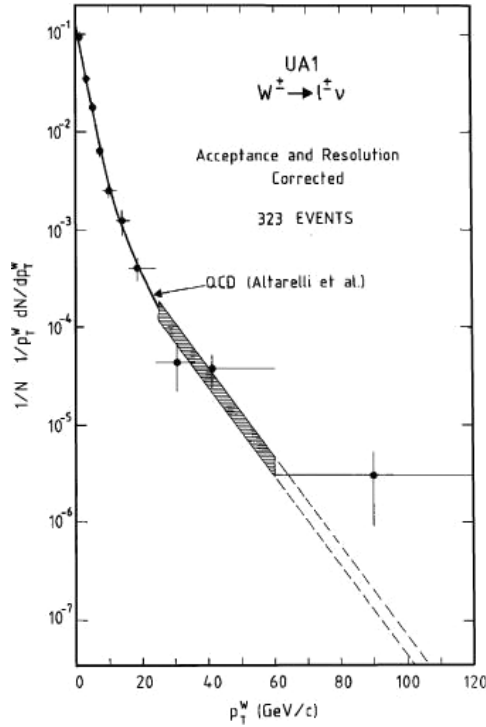


Fig. 23. Distribution of p_T^W , as measured by UA1.¹³ The curve is a QCD prediction,¹⁶ and the shaded band shows the theoretical uncertainty in the region of high p_T^W .

In the UA2 calorimeter jet energies are measured with a resolution $\sigma E/E \approx 0.76/\sqrt{E}$ (E in GeV). The two-jet invariant mass distribution measured by UA2¹⁷ from the data collected between 1983 and 1985 is shown in Fig. 24. This distribution has a clear bump structure in the mass region where two-jet final states from W and Z decays are expected to fall (the bump contains 632 ± 190 events over the continuous background from parton-parton scattering). We note that the ordinates are multiplied by the fifth power of the two-jet mass value in order to remove most of the fast decrease and to use a linear scale. The W and Z peaks are not resolved.

5.5. Precision measurement of the W to Z mass ratio

During the last three years of collider operation (1988–90) UA2 collected large samples of $W \rightarrow e\nu$ and $Z \rightarrow e^+e^-$ decay events. As shown in Subsection 5.1, the systematic error from the uncertainty on the calorimeter energy scale affecting the W and Z masses, as measured by UA1 and UA2 using the 1982–85 data samples, was already comparable to, or even larger than the statistical error. However, the error on the measurement of the ratio m_W/m_Z is mainly statistical, because the systematic uncertainty on the calorimeter energy scale largely cancels in this ratio.

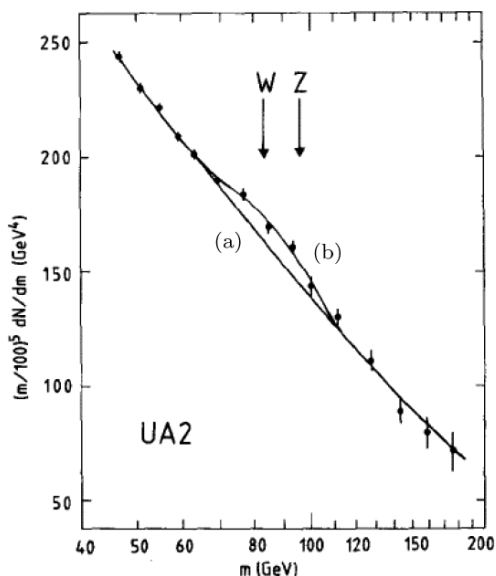


Fig. 24. Two-jet invariant mass distribution, as measured in the UA2 central calorimeter. Curve (a) is a best fit to the data excluding the mass interval $65 < m < 105$ GeV. Curve (b) is a fit to all data points with the addition of two Gaussians centred at the nominal W and Z mass values.

An additional reason for measuring precisely the ratio m_W/m_Z was the start of LEP operation in July 1989, with the expectation that a precise measurement of m_Z would soon become available. Then the two measurements could be combined to obtain a precise determination of m_W .

Figure 25 shows the transverse mass distribution for 2065 $W \rightarrow e\nu$ decays with the electron measured in the UA2 central calorimeter.¹⁸ A best fit to this distribution using m_W as a free parameter gives $m_W = 80.84 \pm 0.22$ GeV (statistical error only).

The measured e^+e^- invariant mass distribution is shown in Fig. 26, which displays two spectra: one containing 95 events in which both electrons fall in a fiducial region of the central calorimeter and their energies are accurately measured; and another spectrum containing 156 events in which one of the two electrons falls outside the fiducial region of the central calorimeter, resulting in a broader mass resolution. Best fits to the two spectra give $m_Z = 91.65 \pm 0.34$ GeV and $m_Z = 92.10 \pm 0.48$ GeV, respectively. The weighted mean of these two values is $m_Z = 91.74 \pm 0.28$ GeV (statistical error only).

The two independent measurements of m_W and m_Z give

$$\frac{m_W}{m_Z} = 0.8813 \pm 0.0036 \pm 0.0019$$

where the first error is statistical and the second one is a small systematic uncertainty which takes into account a possible calorimeter non-linearity.

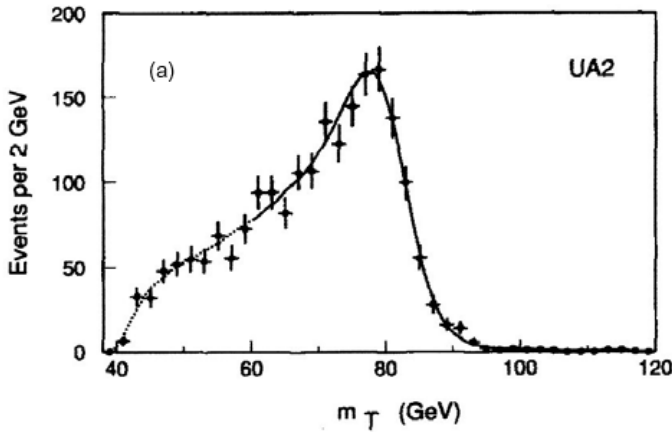


Fig. 25. Transverse mass distribution for 2065 $W \rightarrow e\nu$ decays (see text). The curve is the best fit to the experimental distribution using m_W as a free parameter.

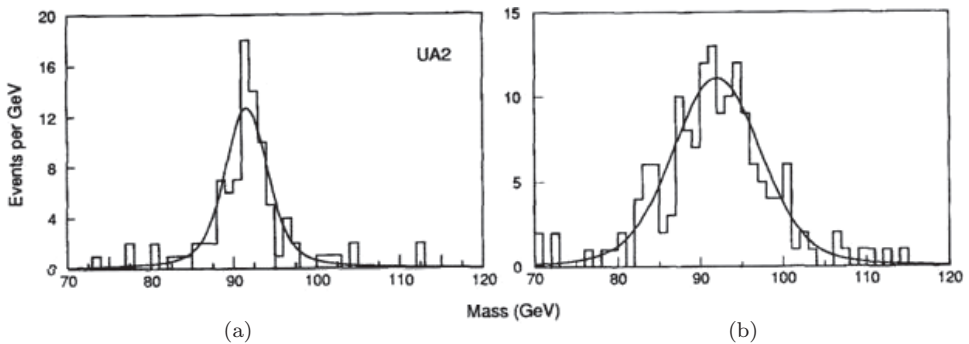


Fig. 26. Invariant mass spectra for two $Z \rightarrow e^+e^-$ event samples, as measured by UA2 (see text). The curves are best fits to the data using m_Z as a free parameter.

By 1991 a precise measurement of m_Z from LEP experiments had become available, $m_Z = 91.175 \pm 0.021$ GeV.¹⁹ Multiplying this value with the ratio m_W/m_Z measured by UA2 provided a determination of m_W with a precision of 0.46%:

$$m_W = 80.35 \pm 0.33 \pm 0.17 \text{ GeV},$$

in agreement with a direct measurement, $m_W = 79.91 \pm 0.39$ GeV, by the CDF experiment at the Fermilab $\bar{p}p$ collider.²⁰

The precise determination of m_W was used to obtain bounds on the top quark mass, for which early direct searches at the CERN and Fermilab $\bar{p}p$ colliders had only provided the lower bound $m_{\text{top}} > 89$ GeV.²¹ As shown by Veltman,²² within the frame of the Standard Model the value of m_W for fixed m_Z depends quadratically on the mass of the top quark through electroweak radiative corrections from virtual fermion loops (and also, to a much smaller extent, on the mass of the Higgs boson).

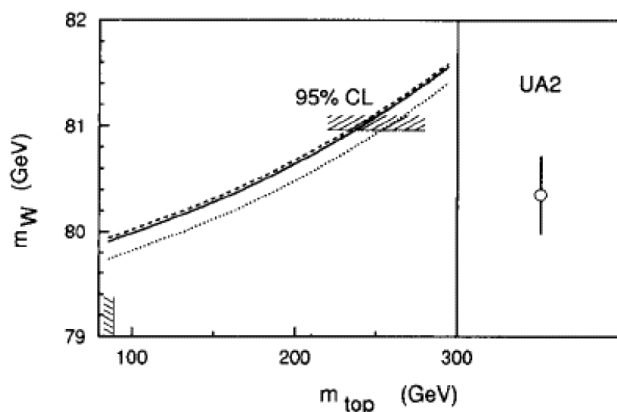


Fig. 27. m_W versus m_{top} and the determination of m_W obtained by combining the precise UA2 measurement of m_W/m_Z with an early precise measurement of m_Z at LEP (see text). The curves are Standard Model predictions for fixed m_Z (as measured at LEP), and for different values of the Higgs boson mass: 50 GeV (dashed curve); 100 GeV (solid curve); and 1000 GeV (dotted curve). Also shown are the 95% confidence level (CL) upper bound $m_{top} < 250$ GeV obtained from the error on m_W , and the lower bound $m_{top} > 89$ GeV from early direct searches at the CERN and Fermilab $\bar{p}p$ colliders.

As illustrated in Fig. 27, the UA2 result gave

$$m_{top} = 160^{+50}_{-60} \text{ GeV},$$

suggesting a heavy top quark well before its discovery at the Fermilab 1.8 TeV collider with a measured mass $m_{top} = 174 \pm 10 \pm 13 \text{ GeV}^{23}$ (the present world average of measurements from the experiments at the Fermilab $\bar{p}p$ collider and, more recently, at the LHC, is $m_{top} = 173.21 \pm 0.51 \pm 0.71 \text{ GeV}^{24}$).

6. Conclusions

The CERN proton–antiproton collider was initially conceived as an experiment to detect the W and Z bosons. Not only it beautifully fulfilled this task, but it also tested the electroweak theory to a level of few percent and provided important verifications of QCD predictions. In the end, it turned out to be a first-class general-purpose accelerator facility with a very rich physics programme. It cannot be excluded that the construction of the LHC would not have been approved if the CERN proton–antiproton collider had not been so successful.

References

1. F. J. Hasert *et al.* *Phys. Lett. B* **46**, 121 (1973); *Phys. Lett. B* **46**, 128 (1973); D. Haidt, *The Discovery of Weak Neutral Currents*, in this book, pp. 165–183.

2. C. Rubbia, P. McIntyre and D. Cline, in *Proc. International Neutrino Conference*, ed. H. Faissner, H. Reither and P. Zerwas, Vieweg, Braunschweig (1977), 683.
3. S. van der Meer, *CERN-ISR-PO* 72-31(1972); S. Van der Meer, *Rev. Mod. Phys.* **57**, 689 (1985).
4. For a review see: L. Jones, F. Mills, A. Sessler, K. Symon and D. Young, *Innovation Is Not Enough: A History of the Midwestern Universities Research Association (MURA)*, (World Scientific, Singapore, 2010).
5. G. Carron *et al.*, *Phys. Lett. B* **77**, 353 (1978).
6. A. Astbury *et al.* (UA1 Collaboration), *Phys. Scripta* **23**, 397 (1981).
7. B. Mansoulié (UA2 Collaboration), in *Proc. Moriond Workshop on Antiproton-Proton Physics and the W Discovery*, La Plagne, Savoie, France, 1983 (Ed. Frontières, 1983), p. 609.
8. For a review see: P. Darriulat and L. Di Lella, *Revealing Partons in Hadrons: From the ISR to the SPS Collider*, in this book, pp. 313–341.
9. G. Arnison *et al.* (UA1 Collaboration), *Phys. Lett. B* **122**, 103 (1983).
10. M. Banner *et al.* (UA2 Collaboration), *Phys. Lett. B* **122**, 476 (1983).
11. G. Arnison *et al.* (UA1 Collaboration), *Phys. Lett. B* **126**, 398 (1983).
12. P. Bagnaia *et al.* (UA2 Collaboration), *Phys. Lett. B* **129**, 130 (1983).
13. C. Albajar *et al.* (UA1 Collaboration), *Z. Phys. C* **44**, 15 (1989).
14. C. Albajar *et al.* (UA1 Collaboration), *Phys. Lett. B* **185**, 233 (1987); and Addendum, *Phys. Lett. B* **191**, 462 (1987).
15. R. Ansari *et al.* (UA2 Collaboration), *Phys. Lett. B* **186**, 440 (1987).
16. G. Altarelli, R. K. Ellis, M. Greco and G. Martinelli, *Nucl. Phys. B* **246**, 12 (1984).
17. R. Ansari *et al.* (UA2 Collaboration), *Phys. Lett. B* **186**, 452 (1987).
18. J. Alitti *et al.* (UA2 Collaboration), *Phys. Lett. B* **276**, 354 (1992).
19. J. Carter, in *Proc. Joint Lepton-Photon Symp. & Europhys. Conf. on High-Energy Physics*, Geneva (Switzerland) 25 July–1 August 1991, (World Scientific, 1992), Vol. 2, p. 3.
20. F. Abe *et al.* (CDF Collaboration), *Phys. Rev D* **43**, 2070 (1991).
21. T. Åkesson *et al.* (UA2 Collaboration), *Z. Phys. C* **46**, 179 (1990); C. Albajar *et al.* (UA1 Collaboration), *Z. Phys. C* **48**, 1 (1990); F. Abe *et al.* (CDF Collaboration), *Phys. Rev. Lett.* **64**, 142 (1990).
22. M. Veltman, *Nucl. Phys. B* **123**, 89 (1977).
23. F. Abe *et al.* (CDF Collaboration), *Phys. Rev. D* **50**, 2966 (1994).
24. K. A. Olive *et al.* (Particle Data Group), *Chin. Phys. C* **38**, 090001 (2014), p. 739.